

Effect of Accessory Attachment on Static Coefficients in a Steel Box Girder for Long-Span Suspension Bridges

Lianjie Liu^{1,2,3*}, Liangliang Zhang^{1,2}, Bo Wu^{1,2} and Ben Chen⁴

¹School of Civil Engineering, Chongqing University, Chongqing 400044, China

²Key Laboratory of New Technology for Construction of Cities in Mountain Area, Chongqing University, Chongqing 400045, China

³Department of Highway Engineering, Chongqing Construction Science Research Institute, Chongqing 400017, China

⁴AECOM, Piscataway, New Jersey 0885, USA

Received 19 December 2016; Accepted 5 February 2017

Abstract

Steel box girders are widely used in long-span suspension bridges nowadays, and static coefficients (drag coefficient, lift coefficient and moment coefficient) are the important parameters in analyzing the aerodynamic stability of bridge girders. A case study of Cuntan Yangtze Suspension Bridge was conducted to study the influence of accessory attachment in steel box girders on their static coefficients. Wind environment was initially measured in site, and then wind tunnel tests of the girder sectional model were performed according to the field measurement. Static coefficients were further calculated by computational fluid dynamics (CFD). In experiments and simulations, the effect of accessory attachment about guard rail ventilation rate and overhaul-dolly rail location on these coefficients was investigated. CFD results were then compared with wind tunnel tests. Results show that even minimal change in this accessory attachment significantly affects the flow distributions. Accordingly, both drag coefficient and lift coefficient are markedly affected within the variation range of about $\pm 30\%$, whereas the moment coefficient is basically not influenced, with the maximum amplitude of variations of $< 2\%$. These data can provide consolidated experimental and numerical simulation basis for future fine aerodynamic analysis and wind-resistance design of such bridge decks.

Keywords: Static coefficient, Flat box girder, Wind tunnel, Computational fluid dynamics (CFD), Accessory attachment

1. Introduction

Exhibiting economical effectiveness, the flat box girder is widely used in long-span suspension bridges [1], [2], [3]. Previous studies showed that this kind of bridges is susceptible to both stationary and non-stationary forces, especially for turbulent wind loads [4], [5]. The stationary forces, such as static forces and moment, can be determined by static coefficients (including drag coefficient, lift coefficient, and moment coefficient) for the subsequent calculation of the aerodynamic admittance functions and aerodynamic stability [6], [7].

With a small slenderness ratio, this type of bridge girder is considered streamlined and semi-aerodynamic. Different from the blunt non-aerodynamic body, whose flow separations take place at the edges and corners, the streamlined body presents uncertain separation positions because of stream velocity, turbulence intensity, girder geometry, surface roughness, and so on [8], [9]. The natural frequencies of these bridges are significantly reduced; therefore, aero-elastic instabilities, such as flutter and vortex-induced vibration, are of the most considerable concern [10], [11]. Therefore, the study of the influence of girder accessory attachment (affiliated members attached to the main girder, including sidewalk railings, and lane guard rails on the upper surface of the bridge girder, overhaul-

dolly rails on the lower surface, and others) on the static coefficients is an interesting and meaningful research topic in wind-resistance design of the long-span suspension bridges with steel box girders.

In general, owing to the complexity of the problem, the limitations of the test facility, and the difficulty of the analytical methods, the effect of the adjustment to the details of girder accessory attachment on static coefficients is usually not investigated to obtain fine aerodynamic stableness in the selection of the cross section of the bridge girder during wind-resistance design [12]. However, according to the theory of fluid mechanics, girder accessory attachment, such as the guard rail shape and overhaul-dolly rail location, can never be ignored. Regardless of their small size relative to the overall size of the bridge girder, these components can significantly affect the static coefficients by changing the flow distribution and controlling the flow separation process. Therefore, under the present circumstances, the accuracy of the final aerodynamic stability design on these long-span suspension bridges will decline if the effect of girder accessory attachment on static coefficients is neglected. With the development of fine wind-resistance design for long-span suspension bridges, extensive research on this issue should be conducted [13].

Based on the above analysis, the present study examines the effect of accessory attachment (involving guard rail ventilation rate and overhaul-dolly rail location) on the static coefficients of a steel box girder for these long-span suspension bridges. Subsequently, the full discussion of the influencing mechanism is included.

2. State of the art

Wind tunnel test and computation fluid dynamics (CFD) simulation are two main methods in wind engineering research [14]. Wind tunnel can obtain the real feature of the problem and can provide indispensable data for CFD validation, whereas CFD can be used to obtain information anywhere in the calculation domain. In the presence of guard rails and overhaul-dolly rails, pressure sensors are impossible to be properly attached in the wind tunnel. In this case, the only practical approach is to measure the global force by a dynamometric balance. However, the influencing mechanism is difficult to understand, without the knowledge of pressure distributions. Under such a poor background, CFD numerical analysis becomes another feasible approach to obtain the aerodynamic characteristics of bridge girders and can provide the pressure information and other flow characteristics surrounding the girder; this information allows a more detailed analysis of the performance affecting factors, as well as the flow–structure interaction mechanism. However, given the sensitivity to the related computational parameters, CFD veracity and reliability is always questionable. Fortunately, valuable guidelines and complementary tips toward accurate and reliable CFD simulations are available [15], [16], [17]. In addition, several literatures to verify and validate the CFD simulation with measurements recently achieved considerable success [18], [19]. These achievements are of substantial significance in the CFD application.

Given that the outermost railings are impermeable in the case study of Tsurumi Fairway Bridge in wind tunnel, the section was considered highly unstable. Railings are required mainly as guard rails for traffic; thus, these railings should be made permeable for better stability. Evidently, modifications to girder structure should be conducted judiciously [20]. Similarly, bird protection barriers on high-speed train bridges exert an impact on the aerodynamic and aero-elastic behaviors of these structures. The most porous barriers with handrails did not substantially modify the aerodynamic loads on the bridge girder. By contrast, barriers with solid screens increase the intensity of these loads significantly in certain cases, and the effect of barriers with solid screen on the airflow around the girder is more evident than that of porous barriers [21]. In addition, the same effect of equipped accessory attachment on the Normandy Cable-stayed Bridge in France was obtained by using CFD in [22]. As found through wind tunnel experiments, the flow pattern near the leading edge is markedly influenced by the depth and height of the simplified horizontal handrail bar. Thus, the corresponding aerodynamic vortex-induced oscillation behavior and pressure distribution of the blunt girder marked changes [23]. In general, the barriers increase the overall degree of bluffness of the section. The main effects of the accessory attachment on the mean values of the aerodynamic forces are the increase in drag force and the decrease in mean lift force [24]. The experimental streamlined bridge girder results show that the aerodynamic modification factors (including stacking loads, crash barriers, vehicles, and central slotting) affecting the aerostatic force coefficients increase the drag force. However, their influences on lift force and torsional moment were minor [25].

According to these studies, shape deviations by the presence or absence of any girder attachment importantly affect the aerodynamic behavior of the girder. However, the effects of further minor modifications, such as the

ventilation rate of the guard rail and the location of the overhaul-dolly rail, were previously clarified or validated sparsely. In terms of aerodynamic characteristics among these studies, bridge girders were simplified by neglecting some of the section details. In addition, few works in the literature combined the two research methods with each other. Therefore, this paper presents a CFD study that is qualitatively validated with wind tunnel test for the effects of guard rail ventilation rate and overhaul-dolly rail location on the aerodynamic performances of the streamlined steel box girder for long-span suspension bridges. Cuntan Yangtze River Bridge is set as an engineering example. Based on the current situation and future development of the bridge wind-resistance, CFD simulations in this study are expected to serve as a complementary tool to the wind tunnel test. The aims of this study are: (a) to obtain the pressure distributions and other flow characteristics around the overall girder for different cases with various configurations and (b) to gain insight into the effect of guard rail ventilation rate and overhaul-dolly rail location on the aerodynamic coefficients of the static forces coefficients.

The remainder of this paper is organized as follows. Section 3 introduces the project case and presents the research methods, including field measurement of wind environment characteristics, wind tunnel facilities, and CFD simulation process. In Section 4, the results are discussed and analyzed. Finally, we conclude the paper and provide certain suggestions in Section 5.

3. Methodology

3.1 Field measurements of wind environment

3.1.1 Case overview

The Cuntan Yangtze Suspension Bridge is located in Chongqing, China, a mountainous city with Zhongliang and Tongluo mountains and Jialing and Yangtze rivers in the middle. The elevation of Chongqing is about 60 m to 800 m. Shown in Fig. 1; the building site of the Cuntan Yangtze Suspension Bridge in Chongqing is a valley and slope landform from the erosion and accumulation for the Yangtze River terrace area. The valley is U-shaped with a width of 840–900 m. The ground elevation ranges from 152 m to 200 m. The south steep slope angle ranges between 15° and 25°, while the north shore slope angle ranges from 15° to 40°. The dominant annual wind direction is north with the frequency of approximately 13%. The annual average wind speed and the annual maximum wind speed are approximately 1.12 and 26.7 m/s respectively according to the local meteorological data.

The Cuntan Yangtze Suspension Bridge is 1520 m in overall length. The main spans crossing the river are 250 m + 880 m + 250 m, with a rise–span ratio of 1/8.8. The distance between two main cable centers is 39.2 m. The structure of the main tower is of the frame gate type. The design driving speed is 80 km/h. The girder is 42 m in width and bears eight bidirectional traffic lanes. The flood design frequency and flood design elevation are 1/300 and 198.40 m, respectively. In addition, the highest and lowest navigable water levels are 193.72 and 156.67 m, respectively. Given a standard height of 10 m, average time interval of 10 min, and recurrence period of 100 years, the design wind speed of the operational phase is 27.5 m/s. Fig. 2 shows the facade and plane arrangement of the bridge. The streamlined

steel box girder with a 42 m width and 3.5 m height (a height–width ratio of 1/12) is applied for the bridge.



Fig. 1. Topography of Cuntan Yangtze Suspension Bridge

3.1.2 In situ setup

Wind environment of the bridge site is the precondition of wind-induced vibration research and the basic data of wind tunnel test. To ensure the accuracy of the wind tunnel test

and CFD numerical simulation, the wind environment parameters should be obtained in advance by field measurements.

As a mountain city, Chongqing exhibits a complex topography, which makes the wind field distribution inconsonant from different regions. The influence of topography on the wind observations is vital. Therefore, the selection of measurement location is particularly important. Such selection should consider topography, weather condition, observation time, and layout content according to the engineering background. The observation equipment should be installed in the main wind direction to reduce the tower shadow effect. The installing position of the device for wind speed and direction will affect the accuracy of the measurement results. To observe the wind characteristics accurately, the wind speed and direction observation equipment should be fixed in a suitable position.

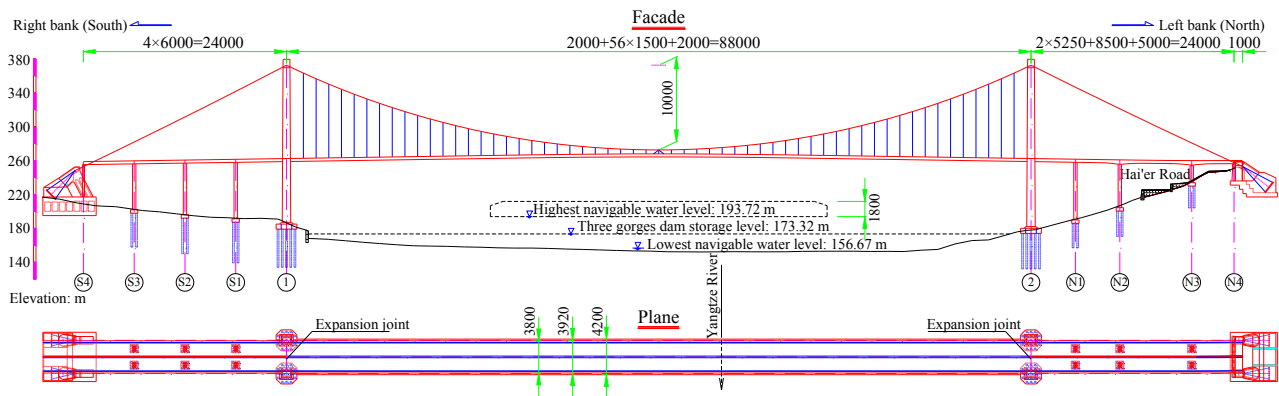


Fig. 2. Facade and plane arrangement of Cuntan Yangtze Suspension Bridge (Unit: cm)

The observation equipment should be fixed on the tower crane in the south shore due to the annual common wind direction, that is, the north wind in Chongqing. Moreover, given the efficiency and convenience of installing the wind observation equipment and the actual situation of the tower crane and bridge pier at the same height in site, such position is preferred. The wind observation system adopts ten sets of observation anemometer equipment, which are installed on the tower crane at 10–100 m-high position. The angle steel bracket holding the anemometer is welded, extending to the river center with a distance of 5 m to avoid the influence of bridge pier and tower crane. Anemometers are installed at the end of the fixed angle steel. The average wind speed is observed by FY-FS wind cup anemometer (Wuhan Fuyuan

Feike Electronic Technology Co., Ltd, China), and the average wind direction is obtained by Yong81000 3D ultrasonic anemometer. The observation layer is arranged at every 10 m, and 10 observation layers are arranged to observe the wind speed profile. Yong81000 ultrasonic anemometer is installed at the height of 10 m. Considering the stability of data transmission, metal conducting wires are used to transmit the data with the acquisition box (600 mm × 400 mm × 200 mm) and solar storage battery at the height of 60 m. Fig. 3 shows the photos of the wind characteristic acquisition equipment. Fig. 4 shows the images of the wind speed and direction acquisition equipment installed on the tower crane.

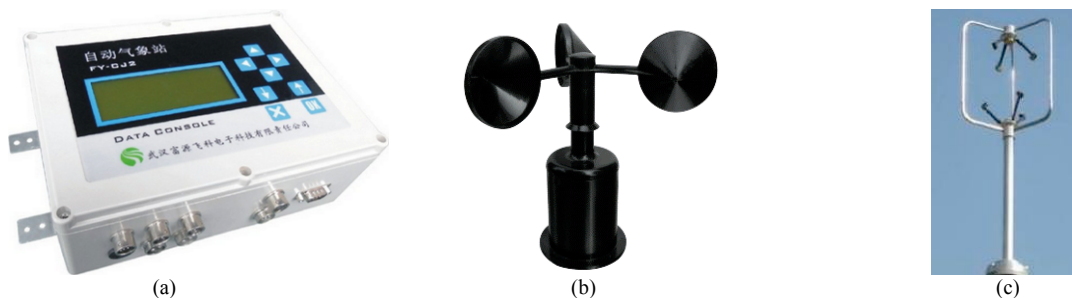


Fig. 3. Photos of wind characteristic acquisition equipment: (a) FY-CJ2 data acquisition equipment, (b) FY-FS cup anemometer, and (c) 3D ultrasonic anemometer

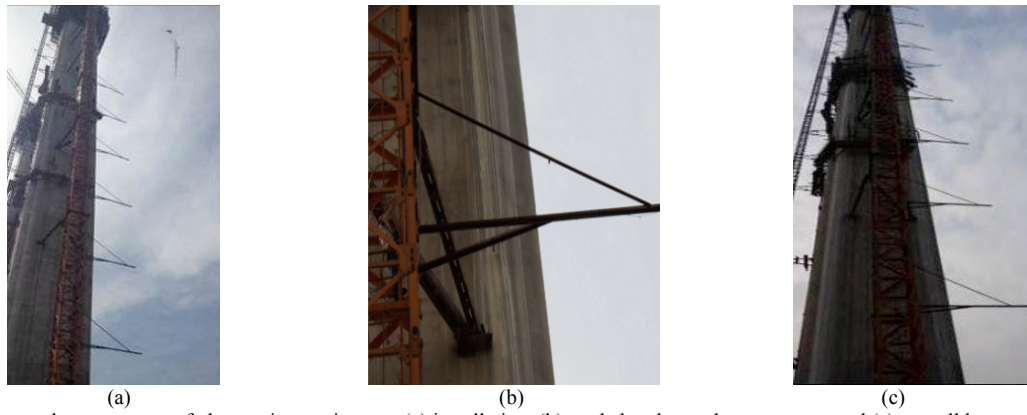


Fig. 4. Installation and arrangement of observation equipment: (a) installation, (b) angle bracket and tower crane, and (c) overall layout

3.1.3 Wind velocity

The wind speed was measured from May 1st, 2014 to April 30th, 2015, which covered a period of one year. The data were collected and processed once a month. Prior to processing of the measurement results, the raw data were pretreated. According to the evaluation by the anemometer, invalid data affected by rainfall or the stabilities of data acquisition system were deleted. The data rate was calculated to ensure that the effective data would be included in the analysis only when they were more than 90%.

The results show low reliability when the basic wind speed for 100-year recurrence period was calculated directly according to the measured data. Therefore, the threshold method was adopted to calculate the peak value, which only needs small sample numbers. This method can reduce the weight of the maximum wind speed and retain many other large wind speeds of the year. Generally, the Generalized Pareto Distribution (GPD) model [26] is commonly used to deal with the probability distribution associated with the cross threshold method. This model can be mathematically expressed in Eq. (1):

$$G(x) = 1 - [1 + c(x - v_s) / b]^{-1/c} \quad (1)$$

where x is the wind speed, v_s is the wind speed threshold, b is the scale parameter, and c is the shape parameter. All these parameters should satisfy Eq. (2).

$$\begin{aligned} b > 0 \\ 1 + c(x - v_s) / b > 0 \end{aligned} \quad (2)$$

Determining the appropriate threshold value is the key of the cross threshold method. For the wind sample $\{v_1, v_2, \dots, v_n\}$, the speed threshold v_s should be sufficiently high for $\{v_i (i = 1, 2, \dots, m \leq n), v_i > v_s\}$ to satisfy the independence requirements. Wind speeds that are more than the threshold follow the normal distribution (Poisson Event). When n tends to infinity, the cross threshold wind speed distribution is the GPD model. To determine the threshold value, the independent individual in the sample should be retained under the premise that the across number obeys the Poisson distribution. In this paper, the wind speed threshold v_s is 6.0 m/s.

For a reasonable range of the given threshold v_s , the GPD model presents stability across the threshold. The distribution parameters of the GPD can be determined, and other parameters of the GPD distribution can be obtained by

the moment features of the variable $y = x - v_s$. The scale b and shape parameter c are expressed in Eqs. (3) and (4), respectively.

$$b = \frac{1}{2} E(Y) \left\{ 1 + \left[\frac{E(Y)}{\sigma(Y)} \right]^2 \right\} \quad (3)$$

$$c = \frac{1}{2} \left\{ 1 - \left[\frac{E(Y)}{\sigma(Y)} \right]^2 \right\} \quad (4)$$

where Y is a cross threshold wind speed sample sequence, E and σ are the expected value and variance of the wind speed samples, respectively.

To calculate the maximum wind speed in the recurrence period of T years, the probability of the maximum wind speed distribution should be determined using Eq. (5):

$$G(v_{\max}) = 1 - 1 / [\lambda(v_s) T] \quad (5)$$

where $\lambda(v_s)$ is the across rate of wind speed, which can be expressed as Eq. (6) in general.

$$\lambda(v_s) = \mu_0 n(v_s) / N \quad (6)$$

where μ_0 is the average annual occurrence rate exceeding the given wind speed (probability of strong wind), $n(v_s)$ is the average number of the extreme wind speed exceeding the threshold v_s , and N is the annual average number exceeding the given wind speed value. Based on the measured wind speed data, Eq. (7) can be obtained by considering $v_s = 6.0$ m/s, $\mu_0 = 0.175$, $N = 51$, and $n(v_s) = 5$ and inserting Eqs. (5) and (6) into Eq. (1):

$$1 - [1 + c(x - v_{\max}) / b]^{-1/c} = 1 - 1 / [\lambda(v_s) T] \quad (7)$$

Therefore, the maximum wind speed can be calculated within the reoccurrence period of T years ($T = 100$). The designed wind speed at the bridge site can be calculated by Eq. (8):

$$v_{\max} = v_s - b \left\{ 1 - [\mu_0 n(v_s) T / N]^c \right\} / c \quad (8)$$

Fig. 5 illustrates the curves of the monthly maximum wind speed and the extreme wind speed at different heights

in different observation periods.

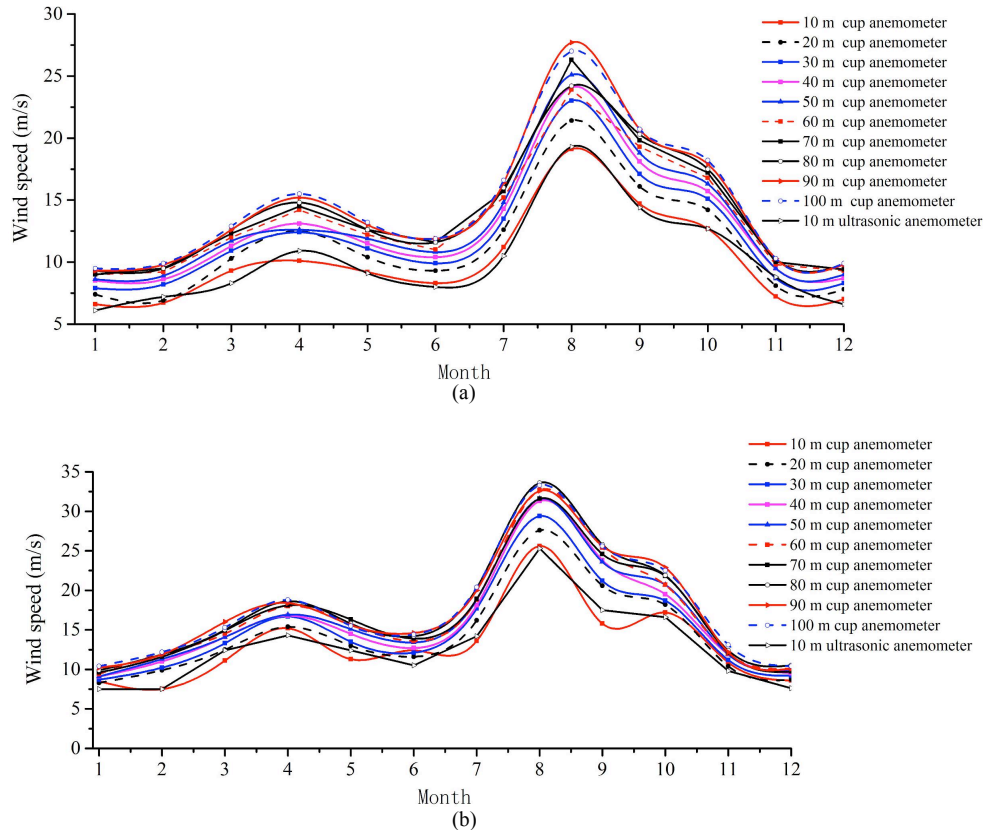


Fig. 5. Monthly observation of maximum and extreme wind speed: (a) monthly maximum wind speed and (b) monthly extreme wind speed

As shown in Fig. 5, the trend of maximum and extreme wind speed for each month increases with height. The maximum wind speed is more regular and obvious than the extreme wind speed. The maximum and extreme wind speeds at 10 and 100 m height are 19.3 and 27.7 m/s and 33.3 and 25.2 m/s, respectively. The maximum wind speed of April, July, August, September, and October all exceeds 10.0 m/s, and those of the remaining months of the year are relatively small. The annual average wind speed of Chongqing is 1.12 m/s according to meteorological data. The measured annual average wind speed of the bridge site is 3.8 m/s. The maximum and extreme wind speeds are about 17.23 and 22.86 times of the meteorological annual average wind speed, respectively. The strong winds mainly concentrate in July–October.

After screening the measured data, 291 groups of the valid data possess the expectation value of $E(Y) = 15.8$ m/s and variance of $\sigma(Y) = 1.51$ m/s. Eq. (8) was used to calculate the measured basic wind speed at Cuntan Yangtze Suspension Bridge site of the 100-year recurrence period, that is, 28.1 m/s.

3.1.4 Wind direction

Based on the statistical analysis of the measured data of the wind direction in a year, the wind rose diagrams of Cuntan Yangtze Suspension Bridge site were obtained. The wind rose diagrams at the height of 10 and 50 m are shown in Fig. 6. Seen from Fig. 6a, the main direction of the wind is north (N) at the height of 10 m with the frequency of 0.254 and the

south wind (S) with the frequency value of 0.112 sequentially. Fig. 6b shows that the main direction of the wind is north northwest (NNW) at the height of 50 m with the frequency of 0.205 and the south-southeast wind (SSE) with the frequency value of 0.101 sequentially. The wind direction distribution varies at different altitudes. The main wind direction moves to the northwest with the increase of height. The main wind direction is N at the height of 10 m, and it changes into NNW at 50 m.

3.1.5 Wind angle

According to the meteorological records of Chongqing, the maximum wind speed on May 2nd, 1985 reaches 36.8 m/s (ten second-level gale) with N wind direction. On June 24th and 25th, 1991, strong winds last for more than two consecutive days with the northeast wind speed of 24.3 (nine-level) and 17.4 m/s (eight-level), respectively. At the time of 2: 25–2: 35 on August 26th, 2014, a strong wind was recorded, and the instantaneous maximum wind speed reaches 25.2 m/s (ten-level), which is rare in Chongqing. Wind speeds over 6.0 m/s, including a total of 1200 data points, were selected in this observation period to analyze the wind angle of attack. The wind attack angle curve and the time history curve of wind speed at the height of 10 m are shown in Fig. 7. The variations in the mean wind speed and wind attack angle at 10 and 50 m on August 26th, 2014 are shown in Fig. 8.

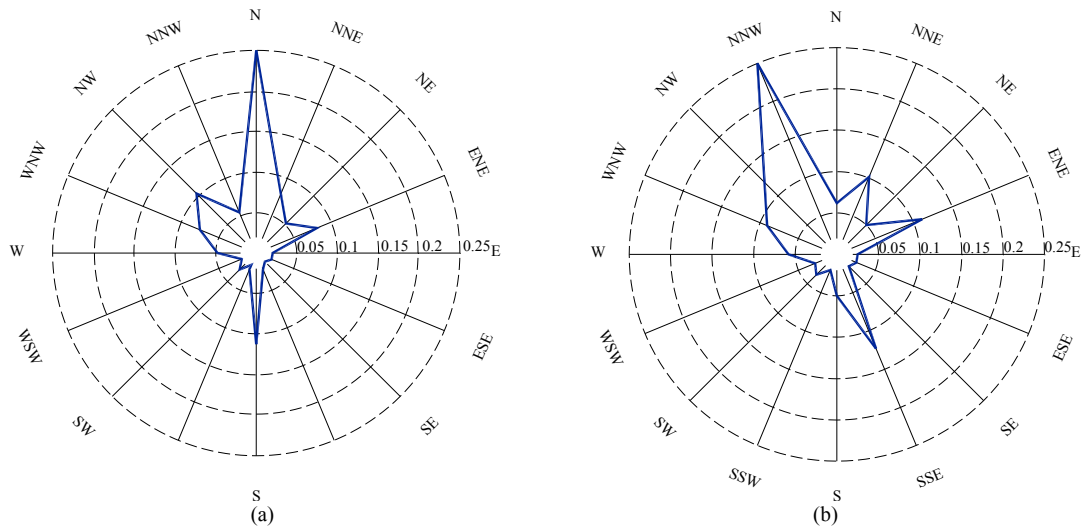


Fig. 6. Wind rose diagrams at different heights: (a) 10 and (b) 50 m

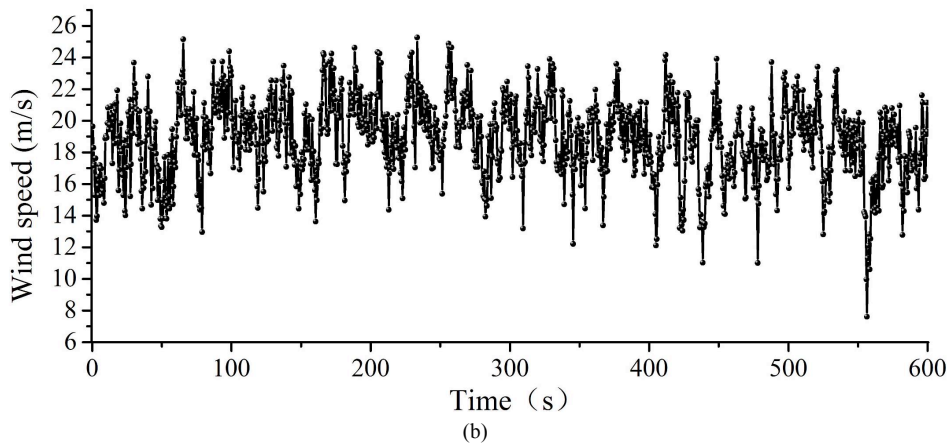
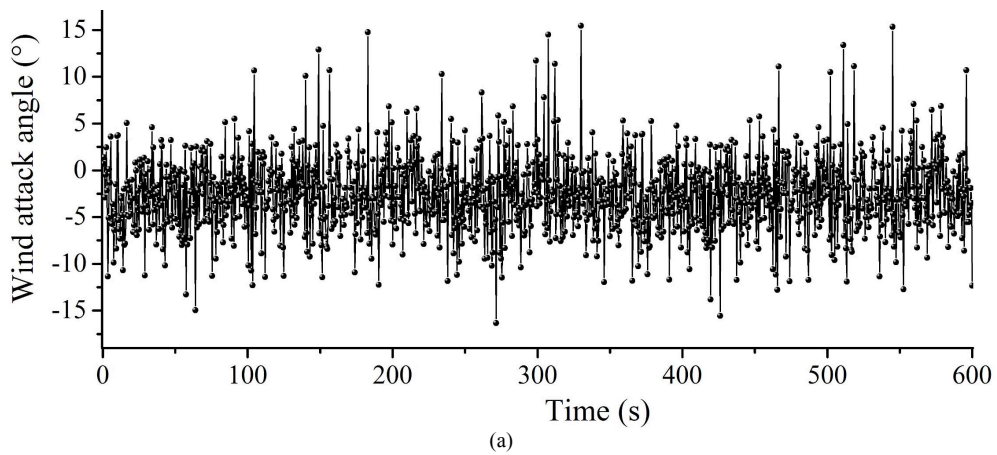
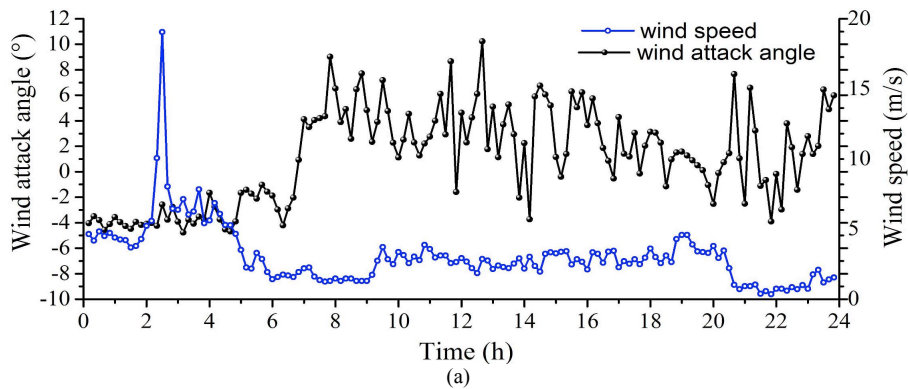


Fig. 7. Curves of wind attack angle and wind speed at 10 m at the time of 2: 25–2: 35, August 26th, 2014: (a) wind attack angle and (b) wind speed



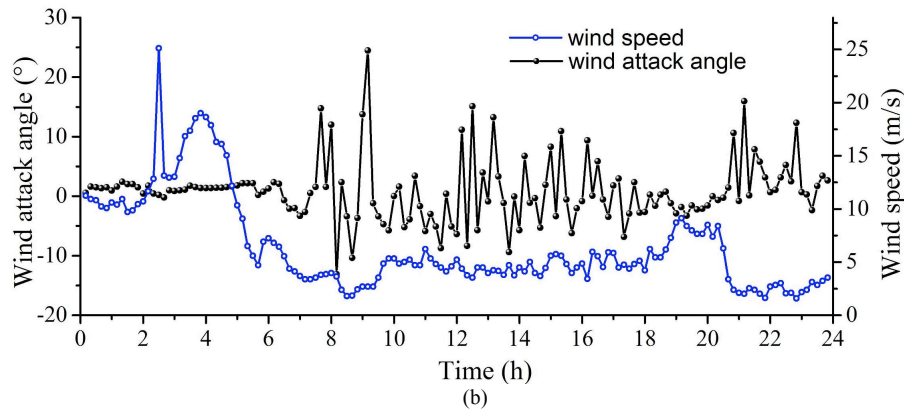


Fig. 8. Mean wind speed and wind attack angle at 10 and 50 m on August 26th, 2014: (a) height of 10 and (b) 50 m

As shown in Fig. 7a, at 2: 25–2: 35 of August 26th, 2014, the maximum wind speed at 10 m of the 10-min mean time interval is 19.3 m/s, and the corresponding 10 min average wind angle of attack is -2.56° with the extreme values of -16.3° and 15.4° . Fig. 7b illustrates that at the same time and date, the maximum value of the 10 min average wind speed at 10 m is 25.1 m/s, and the corresponding 10 min average wind attack angle is 0.1° , with the wind attack angle ranging from -20.4° to 18.7° . Fig. 8a shows the majority of the mean wind attack angle ranges from -10° to -2° , and the majority of the mean wind speed ranges from 5 m/s to 17 m/s at 10 m. Fig. 8b shows the majority of the mean wind attack angle ranges from -12° to $+12^\circ$, and the majority of the mean wind speed ranges from 7 m/s to 20 m/s at 50 m during this time.

The sample for the wind speed data measured in this paper is large. To facilitate the analysis, the average wind speed and wind attack angle at different heights of the 10-min mean time interval during data processing were first calculated based on the original data. Subsequently, the average wind speed and wind angle of attack per day were obtained through the weight average method. Finally, the variation in the average wind speed and wind attack angle at different heights was recognized. The recorded data contained 144 basic time intervals with a total of 172,800 data points. For the mean wind speed over 10.0 m/s during the observation period, the majority of wind angle attack ranges from -12° to $+12^\circ$ at 10 m; the value ranges from -10.4° to 10.1° at 50 m. However, as the wind speed is more than 6.0 m/s, the wind attack angles range from -10.4° to 10.1° at 10 m and from -8.0° to 7.3° at 80 m. Among the samples of the strong wind for 10 min average speed over 6.0 m/s, the corresponding attack angle fluctuates, with the average value of -3.9° .

3.1.6 Summary

The average wind characteristics at Cuntan Yangtze Suspension Bridge site through field measurement can be illustrated as follows: (1) the strong wind is mainly concentrated in the months of July, August, September, and October. The extreme wind speed is remarkably higher than the average wind speed; (2) the wind direction is mainly the N. The wind direction changes with the increase in height. The dominant wind direction moves toward the Northwest; (3) the basic wind speed at the site of the bridge for the 100-year recurrence period is 28.1 m/s, which is higher than the recommended value of 27.5 m/s in the Chinese wind-resistant design guideline for highway bridges; (4) although the range of wind attack angle fluctuates considerably, and

the extreme unusual value in several short periods of time is ignored, the majority wind angle of attack ranges from -12° to $+12^\circ$. All the data from the field measurement provide the basis for the subsequent wind tunnel test and CFD simulation.

3.2 Wind tunnel tests

3.2.1 Test setup

Wind tunnel tests were carried out in the 2nd test section of the Industrial Wind Tunnel in the Southwest Jiaotong University (XNJD-1), Chengdu, China. Fig. 9a presents a photograph of this wind tunnel whose configuration and geometry are shown in Fig. 9c; the overall length is 58.8 m. The dimensions of the test section is $2.4 \text{ m} \times 2.0 \text{ m} \times 16.0 \text{ m}$ (width \times height \times length) with the wind speed adjustable from 0.5 m/s to 45 m/s (turbulent intensity $< 0.5\%$). A balance system mounted on the outside of the wind tunnel was used in the test. The model section was placed in the middle of the test section spanning all the test section width. The incoming wind speed was measured by the hot-wire anemometry sensor shown in Fig. 9b. This sensor comprises an immediate display screen to show the upstream speed instantaneously and resolve the instantaneous vertical and horizontal wind components.

3.2.2 Working case

The detailed dimensions of the standard girder deck for Cuntan Yangtze Suspension Bridge are shown in Fig. 10a. The section model with a scaling ratio of 1: 60 was manufactured using high-quality lightwood and plastic. The length (L), width (B), and depth (H) of the model are 2.095, 0.700, and 0.058 m, respectively. Aerodynamic forces were measured at the ends of the section model using a balance system with three degrees of freedom mounted outside of the wind tunnel wall. The static drag forces, lift forces, and pitching moment were performed under 25 attack angles ranging from -12° to $+12^\circ$ according to the field measurement at an interval of 1° . Three different kinds of pedestrian guard rails (Fig. 10b) were adopted to study the influence of ventilation rate on the aerodynamic coefficients of static forces. The ventilation rates of these guard rails were 59.8%, 45.8%, and 35.6%. With regard to the effect of the location for the overhaul-dolly rails on the static forces, parameter d was introduced to represent the distance between the overhaul-dolly rail and the outer edge of the girder. The overhaul-dolly rails were moved to three

positions of the section model with $d = 0, 2,$ and 4 cm from the outer edge. The corresponding actual size is $0, 1.2,$ and

2.4 m, respectively. Fig. 11 shows the installed section model with details of the wind tunnel.

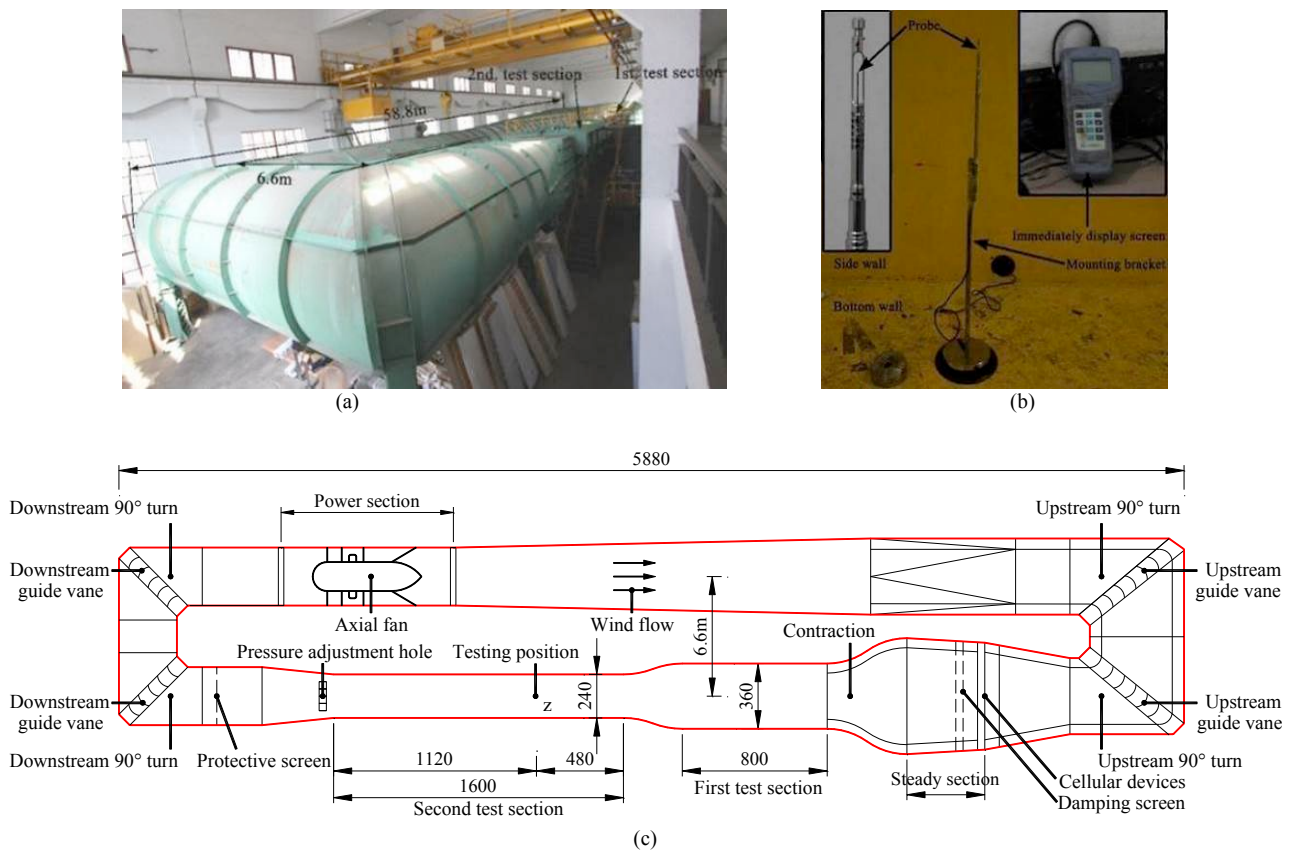


Fig. 9. XNJD-1 Test setup in Southwest Jiaotong University, China: (a) photograph, (b) Hot-wire anemometry sensor, and (c) geometry

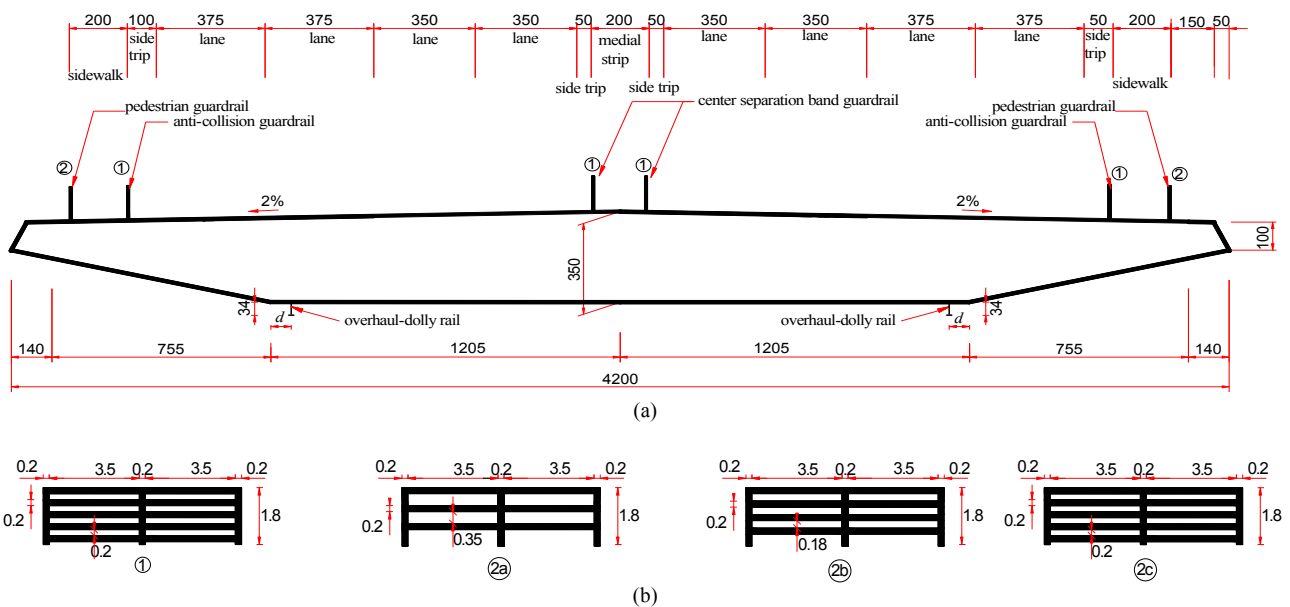


Fig. 10. Accessory attachment: (a) dimensions of standard girder and (b) details of guard rails.

3.3 CFD simulations

3.3.1 Solver settings

The numerical solutions were carried out using ANSYS Fluent 15.0 code. Given that the span-wise shape remains the same, and no significant unsteady phenomena occurs in the wind tunnel test, two-dimensional steady Reynolds-averaged Navier-Stokes equations (2D RANS) were used to compute the mean pressure distributions and aerodynamic forces. According to [27], [28], Menter's shear strain

transport (SST) $k-\omega$ turbulence model shows better agreement with the experimental measurements than those of other turbulence models in simulating pressure distributions and flow separations. To evaluate the discrepancies of static coefficients affected by that girder accessory attachment and provide an insight regarding the flow-structure interaction mechanism in the absence of pressure distribution measurement in wind tunnel test, the SST $k-\omega$ model was adopted because of its ability to reproduce pressure distributions. The pressure-velocity

coupling equations were solved using the semi-implicit method for pressure-linked equation velocity–pressure coupling algorithm with the second-order upwind interpolation of convection item [16]. The uneven distribution of the particles is ignored.

3.3.2 Computational domain and boundary conditions

The 1:60 reduced-scaled model of the geometry for the bridge girder was established. The computational domain was generated by considering 9B before and 13B after the bridge girder section to ensure independence from the boundary inlet condition and allow full development of the

turbulent wake. The geometry, boundary, and meshing diagram are shown in Fig. 12. Boundary conditions were established to reproduce the wind tunnel test conditions. The fluid domain is surrounded by four boundaries. The top and lower parts are symmetric, which allows the reduction of the cells in the entire domain. The incoming flow is inlet-velocity profile, which is normal to the boundary with turbulence intensity of 0.5%, as measured in the wind tunnel test. The downstream is pressure outlet condition, which means that the normal gradients of all dependent variables are zero. In addition, the outer surfaces of the girder model and its subsidiary members are no-slip walls.



Fig. 11. Model section with details: (a) setup and (b) guard rails

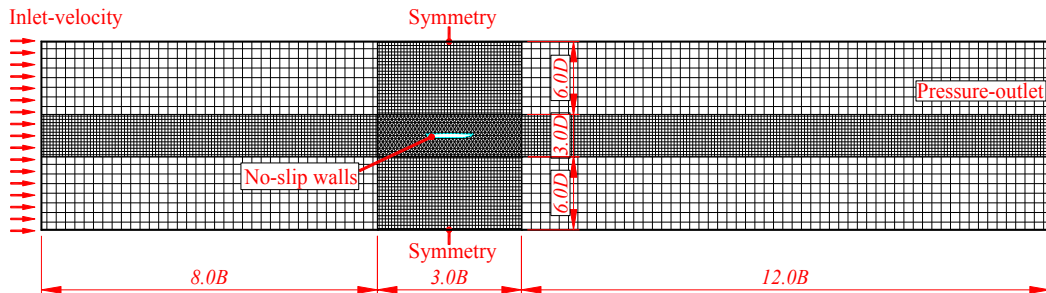
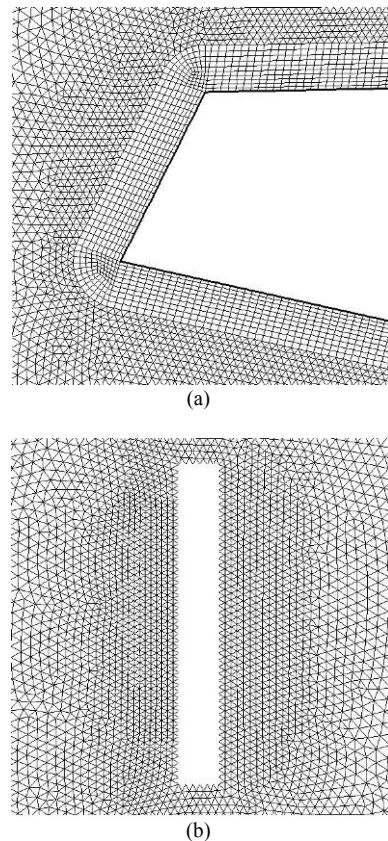


Fig. 12. Geometry, computational domain, and boundary conditions

3.3.3 Meshing

To reduce the numerical error and obtain the optimal performance of the *SST k- ω* model, proper resolution of the boundary layer is a criterion [16]. The mesh spacing between the walls and the first node is 0.1 mm. Another 20 nodes were placed in the boundary layer with a spacing growth ratio of 1.05. Considering accurate simulations of the girder wall, dense grid distribution with 0.05 mm spacing between the wall and the first node was adopted in the boundary layer to achieve a fine particle size. For the remaining regions, small triangular elements were applied in the places where dramatic change of the flow is expected; the size of these elements ranges from 0.1 mm to 17.5 mm, and they are non-structured. Large elements with structured mesh were used for the external regions, and the maximum size is 35 mm. Part of the details regarding the cell distributions around the girder accessory attachment in CFD simulations are shown in Fig. 13.



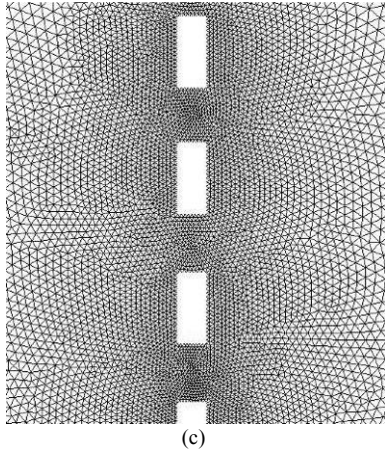


Fig. 13. Cell distributions in CFD: (a) around girder, (b) around lateral guard rail, and (c) around vertical guard rail

4. Result Analysis and Discussion

4.1 CFD versus wind tunnel

To validate the CFD simulations with wind tunnel experimental results, several representative working cases were used as examples for comparison (Table 1). Case **O** is the practical design configuration, and cases **O**, **II_a**, and **II_b** represent the effect of guard rail ventilation rate on the aerodynamic coefficients with cases **O**, **III_a**, and **III_b** reflecting the effect of overhaul-dolly rail location. In the local coordinate system, static coefficients (drag coefficient C_D , lift coefficient C_L , and moment coefficient C_M) are expressed as Eqs. (9) – (11), respectively [27].

$$C_D(\alpha) = \frac{F_D}{0.5\rho U^2 DL} \quad (9)$$

$$C_L(\alpha) = \frac{F_L}{0.5\rho U^2 BL} \quad (10)$$

$$C_M(\alpha) = \frac{M_z}{0.5\rho U^2 B^2 L} \quad (11)$$

where U is the velocity of wind flow; ρ is the wind density (1.225 kg/m^3); F_D , F_L , and M_z are the drag force, lift force, and pitching moment, respectively; B is the girder width; D is the girder height; L is the model length; and α is the

wind attack angle. Sign conventions for forces and pitch rotation moment are shown in Fig. 14.

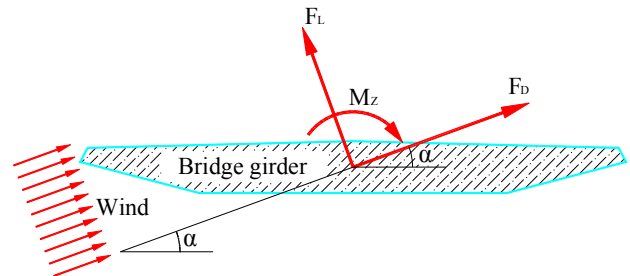


Fig. 14. Aerodynamic force conventions

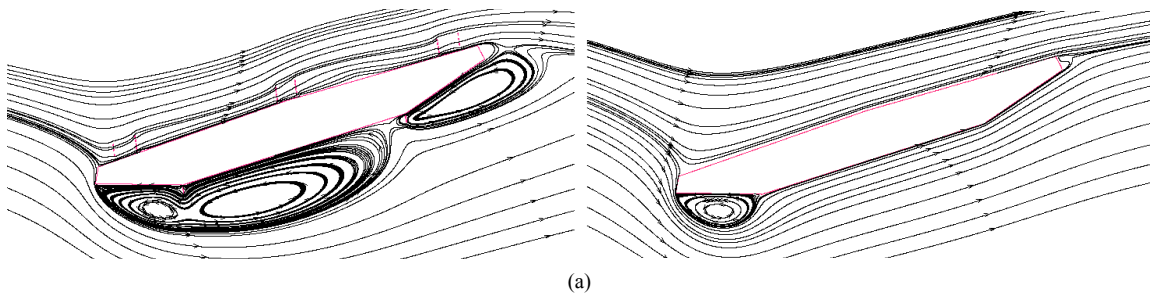
In terms of the trends of C_D , C_L , and C_M as functions of wind attack angle, guard rail ventilation rate, and overhaul-dolly rail location, good agreements exist between CFD and the experimental results. The overall estimated errors of C_D are the smallest, and those of C_M are the largest but still acceptable. As shown in Table 1, the coefficient C_D is mostly affected with an increase of 26% under minimum ventilation rate. In terms of C_L , the maximum variation value is 31% when d is 4 cm. Nevertheless, C_M presents strong inertia with variation range of only 2% during the entire research process.

Table 1. Comparisons between CFD and wind tunnel for several representative working cases ($U = 10 \text{ m/s}$)

Case No.	I_a	I_b	O	II_a	II_b	III_a	III_b
α (°)	-5	0	+5	+5	+5	+5	+5
Ventilation rate (%)	59.8	59.8	59.8	45.8	35.6	59.8	59.8
d (m)	0	0	0	0	0	0.02	0.04
C_D	CFD	1.519	1.320	1.649	1.866	1.937	1.525
	Wind tunnel	1.425	1.389	1.739	2.041	2.195	1.541
C_L	CFD	-0.612	-0.085	0.669	0.684	0.699	0.585
	Wind tunnel	-0.704	-0.093	0.644	0.647	0.668	0.461
C_M	CFD	-0.133	-0.018	0.207	0.166	0.158	0.167
	Wind tunnel	-0.209	-0.011	0.126	0.127	0.126	0.112

4.2 Attack angle

Fig. 15 simulates and depicts the flow characteristics at five attack angles of the streamlined distributions for both the completed girder (deck) states with all the rails and bare deck state without any rail.



(a)

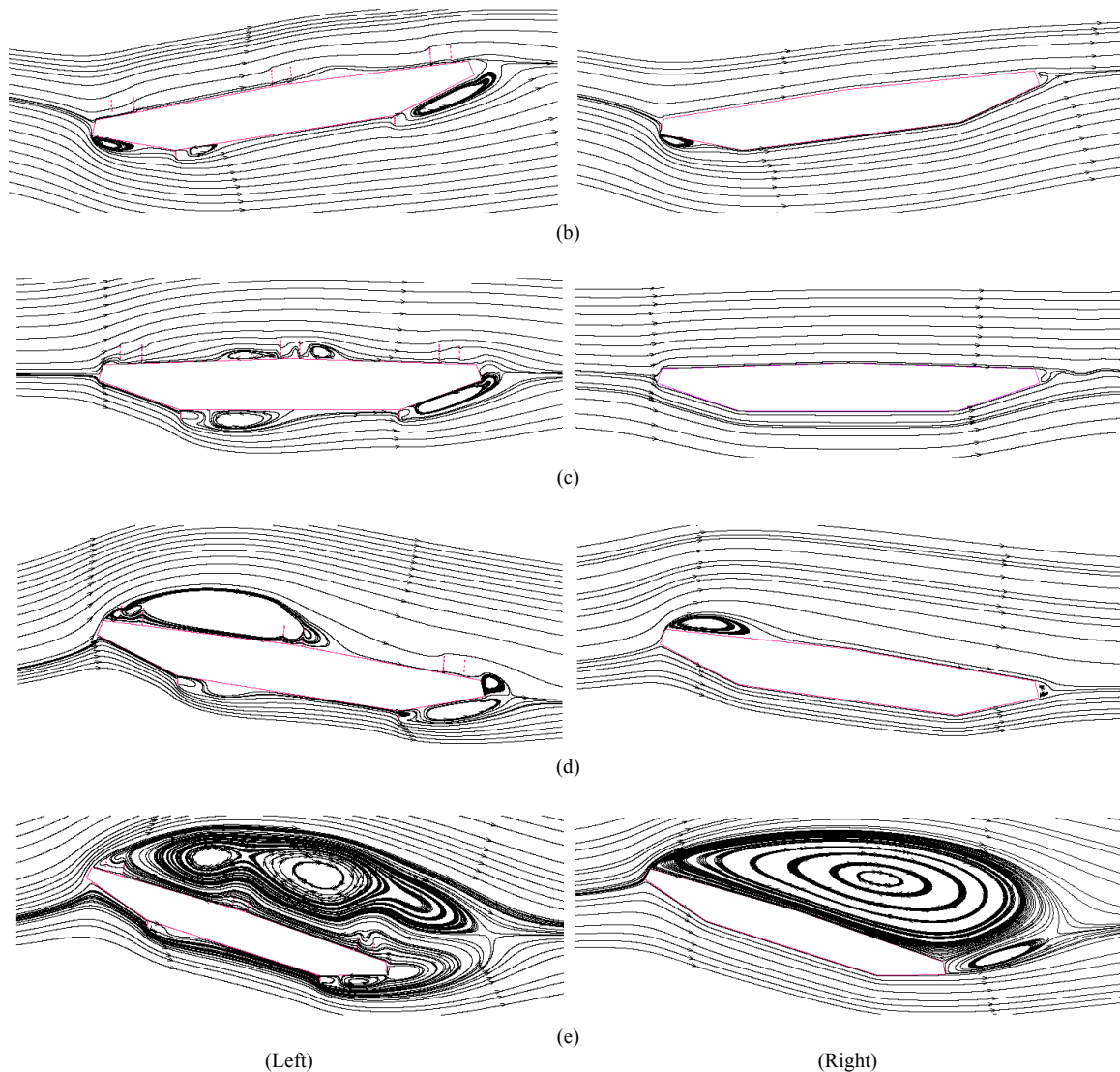


Fig. 15. Streamlined distributions around the different girder states at different attack angles ($U = 10$ m/s): left: ventilation rate = 9.8%, $\alpha = 0^\circ$; and right: bare girder without details

As shown in Fig.15a, all the wind flow attaches to the upper surface for both girders at an extreme negative attack angle of -12° . When the guard rails are exposed directly to the air, the flow above the upper surface is blocked and retarded, which causes an expected increase in the positive pressure according to Bernoulli's equation. At the lower part of the bare girder, a full separation and no reattachment at the trailing edge are observed. However, in the presence of overhaul-dolly rails, the flow separation reattaches the surface between the two overhaul-dolly rails. The second rail behind causes an intensified separation again, thereby resulting in a longer separated length than that of the bare girder. These differences between the two girder states are related with the static coefficients.

Similarly, wind flow remains attached to the upper surface for both girders at a mild negative angle of -6° , as shown in Fig.15b. On the lower surface, a small separation at the leading edge is followed by a smooth reattachment for the bare girder state. Two more separations caused by the two overhaul-dolly rails are observed for the completed girder state, which results in an intermittent reattachment.

Fig.15c shows that in the most common case of the attack angle of 0° , the bare girder shows the superior performance of the streamlined shape, where the flow attaches to both the top and lower surfaces. Nevertheless, in

the presence of guard rails and overhaul-dolly rails, the flow is intercepted discontinuously. Consequently, small flow separations are observed in the vicinity of these rails.

At the positive angle of 6° , Fig.15d shows an increasing small separation on the upper surface of the leading edge in the bare girder. Subsequently, a reattachment is shown near the middle width of the section. However, for the completed girder state, the flow separation on the upper surface is intensified by the first guard rail, which increases the length of the separated flow. An initial positive pressure region, followed by several small separations with negative pressures, is observed on the lower surface of the completed girder and that of the attached flow is mild positive pressures for the bare state.

Under the extreme positive angle $+12^\circ$ shown in Fig.15e, the full separation without reattachment on the upper surface is observed for both girders. The guard rails intensify the separation on the upper surface, and the overhaul-dolly rails remain and cause several small separations on the lower surface. Similar to that of the -12° , the flow on the lower surface is retarded by the rails. Thus, an increase in the positive pressure is expected.

The static coefficients as the function of the wind attack angle are shown in Fig.16. Afterward, the following analysis and discussion can be carried out:

(1) As shown in Fig. 16a, in the completed girder state, the drag coefficient C_D shows an initial decrease when the attack angle moves to the positive; this observation may be due to the tilting of the girder extending the contact area. The same phenomenon is observed for the bare girder state without girder accessory attachment. Therefore, C_D decreases an overall level of 30%–40% in magnitude because of the absence of these section details.

(2) The lift force F_L is caused by the pressure difference between the upper and lower surfaces of the girder. At the negative attack angles, the separation bubbles in negative pressures occur on the lower surface of the girder. The positive pressure on the upper surface is considered, and negative lift forces are yielded. When the attack angles move positively, the separation bubbles become small, which decreases the pressure differences between the upper and lower surfaces. Fig. 16b shows that the lift coefficient C_L decreases in magnitude, and a positive slope is observed. Under the positive attack angles, the separation bubbles occur on the upper surface. Hence, the negative C_L is supposed to change its sign at the attack angle of 0° . However, given that the girder are asymmetric in the vertical direction, an accelerated flow over the streamlined lower surface is observed, thereby resulting in larger negative pressure of the lower surface than that of the top. Consequently, C_L is negative. C_L is always negative until the attack angle of 3° when the separation bubble on the upwind incoming region is expected to counterbalance the negative pressure below the lower surface. The separation bubble on the upper surface expands in area with the increasing strength of the attack angle and positively contributes to C_L . Comparison of the magnitude of C_L between the two states shows the remarkably small slope recorded for the bare girder state at strong attack angles. Accordingly, this small slope should attribute to the high positive pressures caused by the section details on the upper surface (for negative angles) or on the lower surface (for positive angles).

(3) The pitching moment is caused by the pressure differences between the upwind upper portion and the downwind lower portion. The negative pressure zone appears and expands above the upwind upper surface because of the increasing angle, thereby increasing the pressure difference. Such difference contributes positively to the moment coefficient C_M . Consequently, Fig. 16c shows that C_M increases naturally with the increase of the attack angle. The influence of the guard rails and overhaul-dolly rails on C_M is approximately negligible. Possible reason is the symmetry of these details in the horizontal direction, which results in simultaneous influence on both the upwind and downwind pressure distributions.

4.3 Guard rail ventilation rate

The static coefficients in relation to the guard rail ventilation rate as the function of the wind attack angle are shown in Fig. 17. The following insights can be drawn: (1). According to Fig. 17a, the drag coefficient C_D increases with decreasing ventilation rate; for small angles, this trend is more obvious than that of strong angles; (2). In Fig. 17b, the lift coefficient C_L increases for these positive attack angles when the ventilation rate decreases. On the contrary, it increases in

magnitude at negative attack angles with the negative sign, which means a large slope; (3). The maximum contribution of the decreasing ventilation rate to C_M is less than 0.02, which indicates a negligible influence (Fig. 17c).

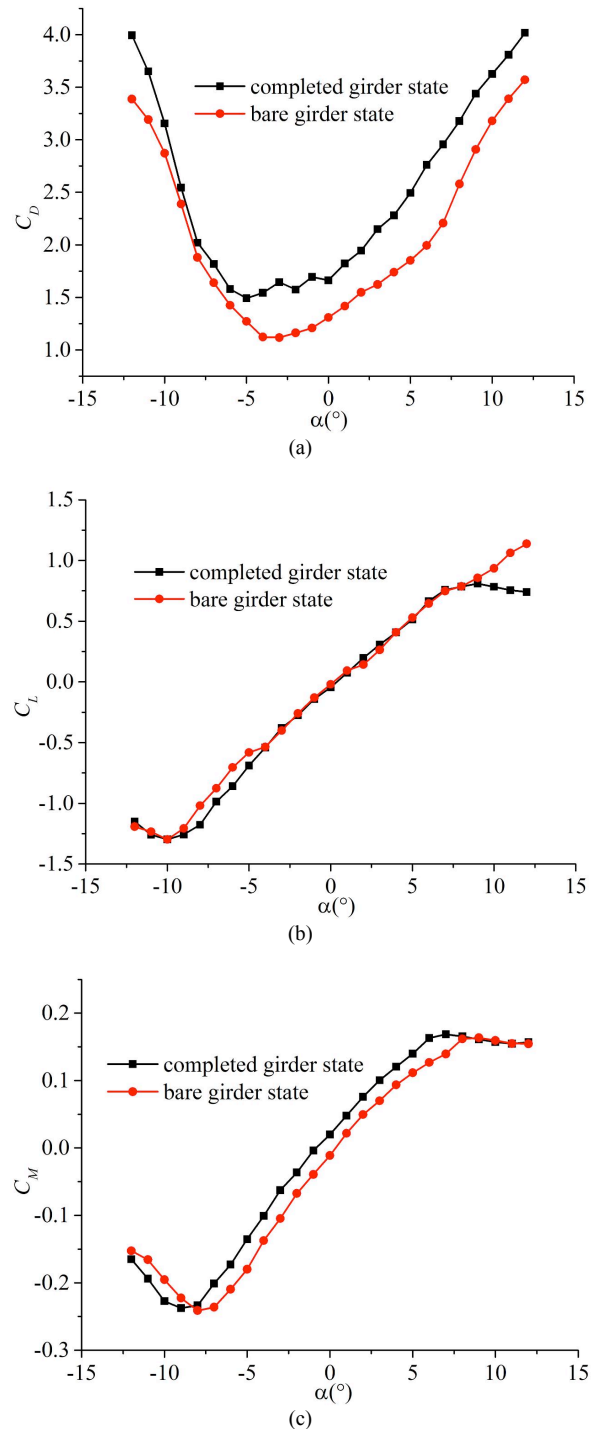


Fig. 16. Static coefficients as function of wind attack angle ($U = 10$ m/s): (a) $C_D(\alpha)$, (b) $C_L(\alpha)$, and (c) $C_M(\alpha)$

Considering that these girder configurations were investigated at 25 attack angles ranging from -12° to $+12^\circ$, the case of $+5^\circ$ was used to obtain an accurate understanding of the influence mechanism. Pressure coefficient C_p is defined as in Eq. (12).

$$C_p = (P_i - P_\infty) / [0.5\rho U^2] \quad (12)$$

where P_i is the static pressure at the measuring point, and P_∞ is the reference static pressure. C_p is depicted normal to the outside surface of the girder for negative pressures and inside for the positive ones. Concerning the cases O , II_a , and II_b , which represent three different ventilation rates, Fig. 18 shows the pressure coefficient C_p on upper and lower surfaces as the function of x/B . Possible variation mechanism of the aerodynamic coefficients can be explained as follows.

(1) An increasing separation on the upper surface of the leading edge and subsequent smooth reattachment are observed. When the ventilation rate is decreased from case O to case II_a , the wind-rail interactions become intense and complicated, which results in high angle-of-separation, a high separation bubble, a long reattachment length, and a wide wake zone. Consequently, C_D increases. Given that the wind-rail interactions are nearly vertical, the decrease of ventilation rate for small attack angles causes more significant positive contribution to C_D than that of strong angles.

(2) In cases of positive attack angles, a wide and high separation bubble with negative pressure is caused by the decreasing ventilation rate, which leads to a fast and strong backflow in the bubble. According to Bernoulli's equation, the decrease in pressure is caused by the increase in flow velocity, which theoretically explains the phenomenon that the pressure coefficient C_p of the upper surface decreases with decreasing ventilation rate. The C_p in the lower surface is unanimous; considering that the lift force F_L is caused by the balance between the pressure of the upper and lower surfaces, C_L increases when the ventilation rate decreases from case O to case II_b .

(3) In the cases of negative attack angles, the separation occurs at the lower surface, instead of the upper one. The changes of the rails on the upper surface exert little influence on the pressure distributions of the lower surface. When the upper surface is in the positive pressure, and the ventilation rate decreases from case O to case II_b , the flow-rail interaction becomes intense. Consequently, the flow velocity is low, which results in an increase in the positive pressures according to Bernoulli's equation. Moreover, the negative lift force decreases in magnitude.

4.4 Overhaul-dolly rail location

The static coefficients in relation to the overhaul-dolly rail location at different attack angles are shown in Fig. 19. The following insights can then be drawn: (1). When d increases in Fig. 19a, *i.e.*, the overhaul-dolly rails move inward, and the drag coefficient C_D decreases at positive attack angles, which is negligible at negative attack angles; (2). When d increases in Fig. 19b, the lift coefficient C_L decreases at positive attack angles, which is negligible at negative attack angles; (3). The variation of C_M affected by the increase of d is approximately negligible, as shown in Fig. 19c.

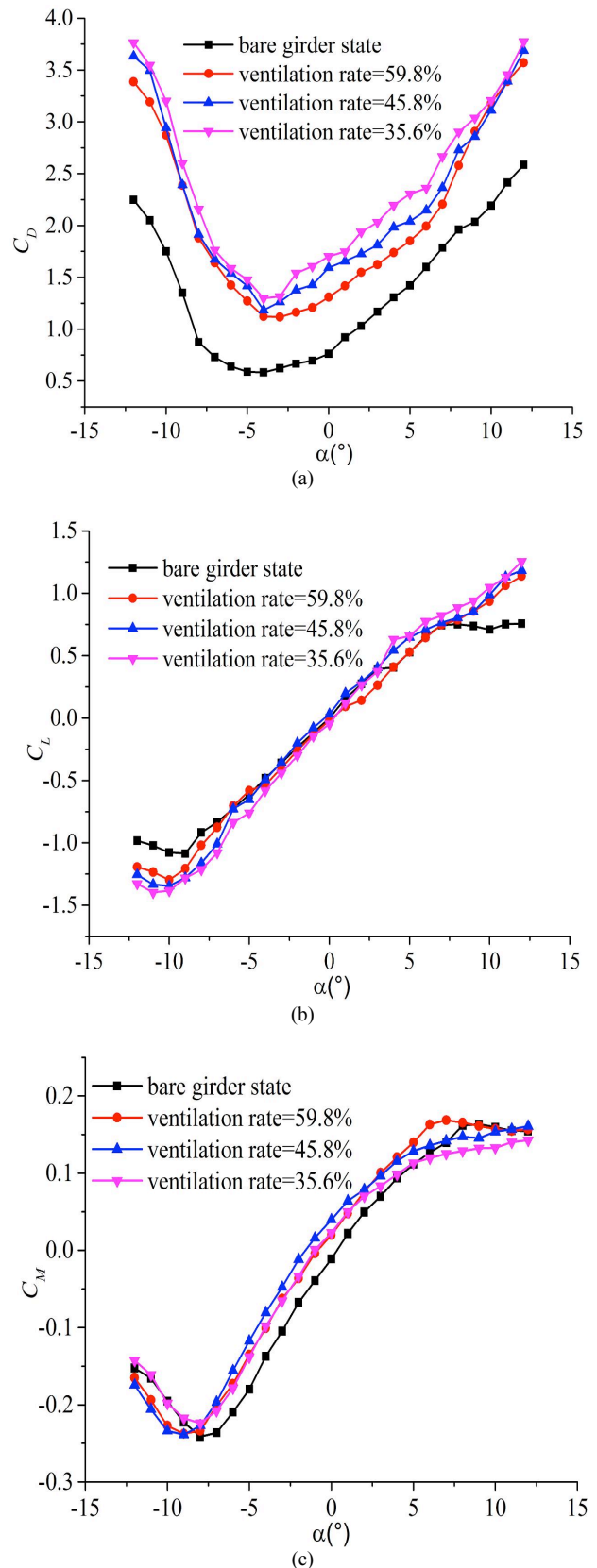


Fig. 17. Static coefficients relating guard rail ventilation rate ($d = 0$, $U = 10\text{m/s}$): (a) $C_D(\alpha)$, (b) $C_L(\alpha)$, and (c) $C_M(\alpha)$

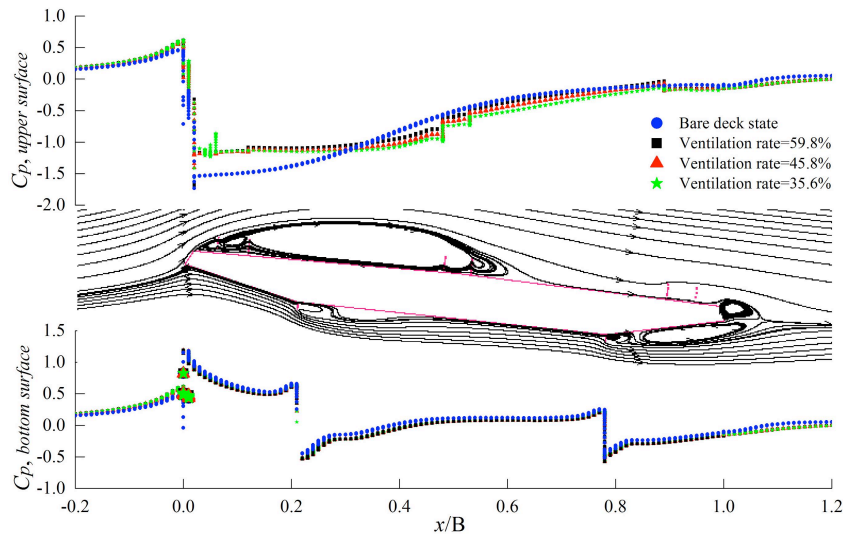


Fig. 18. Influence of guard rail ventilation rate on mean pressure coefficient distributions ($\alpha = +5^\circ$)

The configurations at $+5^\circ$ were selected to explain the variations from a numerical point of view. Fig. 20 shows the pressure coefficient of both upper and lower surfaces for cases *O*, *III_a*, and *III_b*, which represent three different locations of overhaul-dolly rails. Possible variation mechanism can be explained as follows:

(1) At positive attack angles, small separations on the lower surface start at a farther point from the leading edge and stop at a closer point from the trailing edge when the overhaul-dolly rails move inward. Accordingly, the separation bubble and the wake zone both sink. In addition, the leading portion of the girder becomes streamlined due to the inward movement of the overhaul-dolly rails, thereby weakening the wind-rail interactions. Accordingly, the drag force decreases. The weakening of wind-rail interactions also results in a large flow velocity. Therefore, a small positive pressure on the lower surface is expected. The positive lift force decreases with respect to the balance between the pressure on the upper and lower surfaces.

(2) At negative attack angles, separations occur on the lower surface of the leading edge portion. When the overhaul-dolly rails are immersed in the wake of leading edge, their small movements contribute slightly to the flow field on the lower surface. Considering the pressure distribution on the upper surface that is independent from the modifications on the lower surface, the static forces and moments are approximately constant with the movements of overhaul-dolly rails at negative attack angles.

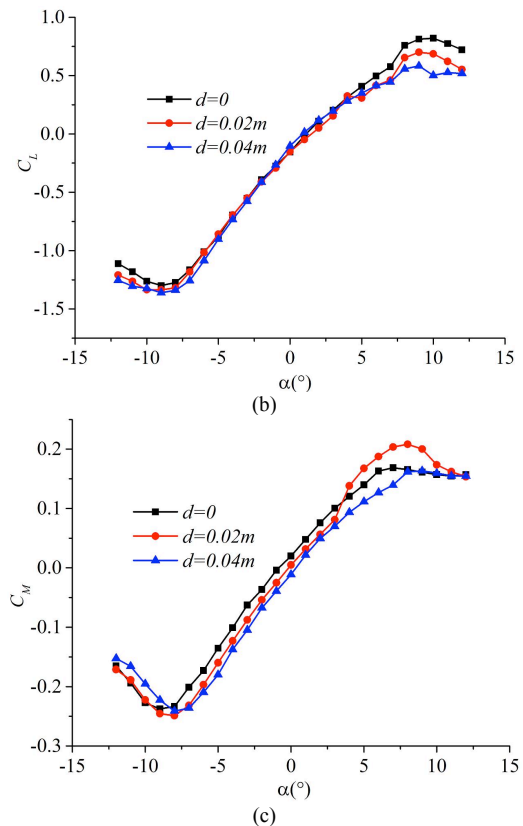
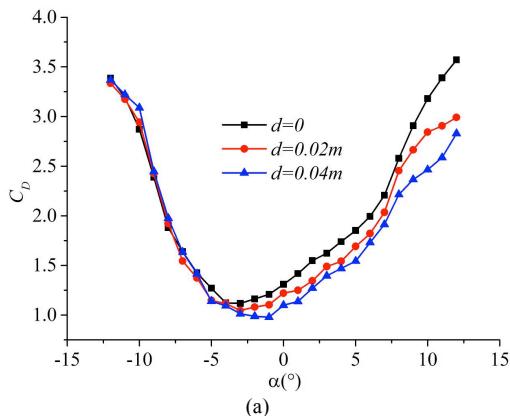


Fig. 19. Static coefficients relating overhaul-dolly rail location (Ventilation rate = 59.8%, $U = 10$ m/s): (a) $C_D(\alpha)$, (b) $C_L(\alpha)$, and (c) $C_M(\alpha)$

5. Conclusions

A case study was carried out on Cuntan Yangtze Suspension Bridge to evaluate the effect of accessory attachment (including guard rail ventilation rate and overhaul-dolly rail location) in steel box girders on their static coefficients for long-span suspension bridges. The actual wind environment parameters of the bridge site were measured in situ. The wind conditions for experiments and simulations were provided. Change rules of static coefficients for the bridge girder were investigated in wind tunnel test. CFD simulation and analysis model of the bridge girder were established according to the 2D RANS equations and SST $k-\omega$ turbulence

principle. Finally, the following conclusions were drawn.

(1) The decrease in guard rail ventilation rate increases the wind blockage area, which expands the wake zone and increases the value of the drag coefficient. Furthermore, the negative pressure range in positive attack angles expands,

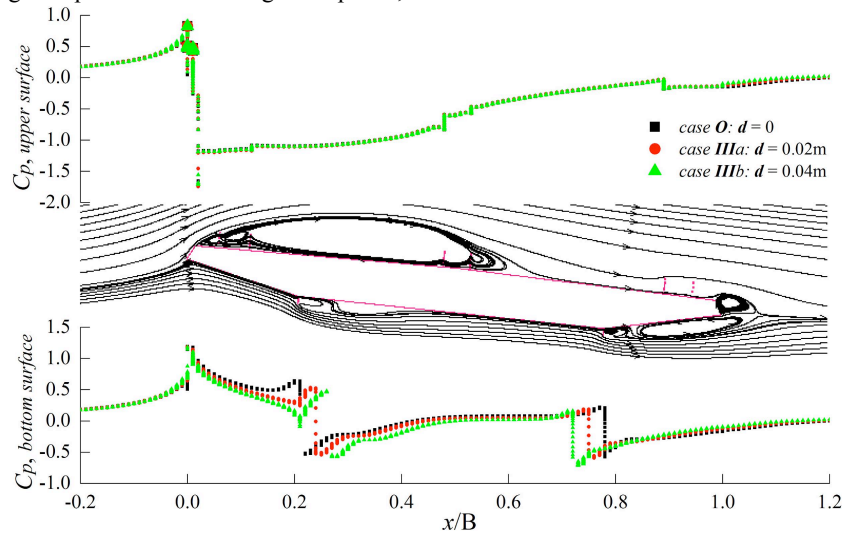


Fig. 20. Influence of overhaul-dolly rail location on mean pressure coefficient distributions ($\alpha = +5^\circ$)

(2) When the overhaul-dolly rails are moved inward during positive attack angles, the blunt degree of the cross section is weakened, which decreases both the negative pressure and wake zones. Consequently, both the drag and lift coefficients decrease. However, the variation in separation and reattachment is minor when the location of the overhaul-dolly rail changes in negative attack angles. Thus, neither the drag coefficient nor the lift coefficient presents a significant fluctuation.

(3) When the wind attack angle moves from negative to positive, the drag coefficient initially decreases to the right and subsequently increases when the wind attack angle is approximately -3° . The lift coefficient presents a continuous increasing trend.

(4) The changes of the moment coefficient with the variation of the guard rail ventilation rate and the overhaul-dolly rail location are generally negligible.

These findings confirmed how variations in accessory attachment influence the characteristics of flow around the streamlined flat box girder and change the corresponding

static coefficients. Therefore, the effect should not be ignored during the wind-resistance design of long-span suspension bridges. Nevertheless, the static coefficients can be affected by many factors. The present findings are only limited to the effect of guard rail ventilation rate and overhaul-dolly rail location. Other influencing factors should be considered in future studies.

case O: $d = 0$

case IIIa: $d = 0.02\text{m}$

case IIIb: $d = 0.04\text{m}$

static coefficients. Therefore, the effect should not be ignored during the wind-resistance design of long-span suspension bridges. Nevertheless, the static coefficients can be affected by many factors. The present findings are only limited to the effect of guard rail ventilation rate and overhaul-dolly rail location. Other influencing factors should be considered in future studies.

Acknowledgements

This work was supported by both the National Natural Science Foundation of China (No.51578098) and the Science Foundation of Chongqing Municipal Urban-Rural Development Commission (No.20130844). This work was also sponsored by AECOM in New Jersey of USA.

This is an Open Access article distributed under the terms of the Creative Commons Attribution Licence



References

- Wang, R., Li, G., "Numerical simulation for the residual stress of u-rib welding onto the flat steel box girder". *Journal of Civil Architectural and Environmental Engineering*, 37(1), 2015, pp.104-111.
- Yang, Y., Zhang, L. L., Wu, B., Ling, X., "Vehicle effect on vortex-induced vibration of flat steel box girder". *Open Civil Engineering Journal*, 10(1), 2016, pp.12-14.
- Liu, L. J., Zhang, L. L., Wu, B., Yang, Y., "Aerodynamic admittance research on wide-body flat steel box girder". *Open Civil Engineering Journal*, 10(1), 2016, pp.891-904.
- Huang, W., Zou, K., "Non-stationary buffeting response analysis of long span suspension bridge under strong wind loading". *Journal of Harbin Institute of Technology (New Series)*, 23(6), 2016, pp.9-16.
- Zhou, R., Yang, Y., Zhang, L., Ge, Y., "Interference effect on stationary aerodynamic performance between parallel bridges". *International Journal of Structural Stability and Dynamics*, 16(10), 2016, pp.1750017/1-23.
- Zhao, X., Gouder, K., Graham, J. M. R., Limebeer, D. J. N., "Buffet loading, dynamic response and aerodynamic control of a suspension bridge in a turbulent wind". *Journal of Fluids and Structures*, 62, 2016, pp.384-412.
- Song, L., Fu, S., Dai, S., Zhang, M., Chen, Y., "Distribution of drag force coefficient along a flexible riser undergoing viv in sheared flow". *Ocean Engineering*, 126, 2016, pp.1-11.
- Lee, C. H., "Flow field analysis on the stagnation streamline of a blunt body". *International Journal of Aeronautical and Space Sciences*, 17(2), 2016, pp.149-156.
- Xu, K., Zhao, L., Cao, S. Y., Yoshida, A., Tamura, Y., Ge, Y. J., "Investigation of spatial coherences of aerodynamic loads on a streamlined bridge deck in an actively-controlled wind tunnel". *Advances in Structural Engineering*, 17(1), 2014, pp.53-66.
- Zhang, W. W., Li, X. T., Ye, Z. Y., Jiang, Y. W., "Mechanism of frequency lock-in in vortex-induced vibrations at low Reynolds numbers". *Journal of Fluid Mechanics*, 783, 2015, pp.72-102.
- Li, Y. L., Zhu, J. Q., Tang, H. J., "Aeroelastic simulation of vortex-induced vibration and flutter based on CFD/CSD coupling solution". *Journal of Vibration and Shock*, 34(12), 2015, pp.85-89 and 114.
- Fujino, Y., Siringoringo, D., "Vibration mechanisms and controls of long-span bridges: A review". *Structural Engineering International Journal of the International Association for Bridge and Structural Engineering*, 23(3), 2013, pp.2013.

13. Vairo, G., "A simple analytical approach to the aeroelastic stability problem of long-span cable-stayed bridges". *International Journal for Computational Methods in Engineering Science and Mechanics*, 11(1), 2010, pp.1-19.
14. Yu, M., Liao, H. L., Li, M. S., Ma, C. M., Luo, N., Liu, M., "Study on static wind loading coefficients of suspension bridge based on CFD simulation and wind tunnel test". *Applied Mechanics and Materials*, 66-68, 2011, pp.334-339.
15. Rong, L., Nielsen, P. V., Bjerg, B., Zhang, G., "Summary of best guidelines and validation of CFD modeling in livestock buildings to ensure prediction quality". *Computers and Electronics in Agriculture*, 121, 2016, pp.180-190.
16. Blocken, B., "Computational fluid dynamics for urban physics: Importance, scales, possibilities, limitations and ten tips and tricks towards accurate and reliable simulations". *Building and Environment*, 91, 2015, pp.219-245.
17. Blocken, B., Gualtieri, C., "Ten iterative steps for model development and evaluation applied to computational fluid dynamics for environmental fluid mechanics". *Environmental Modelling and Software*, 33, 2012, pp.1-22.
18. Abbas, T., Morgenthal, G., "Framework for sensitivity and uncertainty quantification in the flutter assessment of bridges". *Probabilistic Engineering Mechanics*, 43, 2016, pp.91-105.
19. Blocken, B., van der Hout, A., Dekker, J., Weiler, O., "CFD simulation of wind flow over natural complex terrain: Case study with validation by field measurements for ria de ferrol, galicia, spain". *Journal of Wind Engineering and Industrial Aerodynamics*, 147, 2015, pp.43-57.
20. Jones, N. P., Scanlan, R. H., Sarkar, P. P., Singha, L., "The effect of section model details on aeroelastic parameters". *Journal of Wind Engineering & Industrial Aerodynamics*, 54-55(94), 1995, pp.45-53.
21. Ogueta-Gutiérrez, M., Franchini, S., Alonso, G., "Effects of bird protection barriers on the aerodynamic and aeroelastic behaviour of high speed train bridges". *Engineering Structures*, 81, 2014, pp.22-34.
22. Bruno, L., Khris, S., Marcillat, J., "Numerical simulation of the effect of section details and partial streamlining on the aerodynamics of bridge decks". *Wind And Structures An International Journal*, 4(4), 2001, pp.797-802.
23. Nagao, F., Utsunomiya, H., Yoshioka, E., Ikeuchi, A., Kobayashi, H., "Effects of handrails on separated shear flow and vortex-induced oscillation". *Journal of Wind Engineering and Industrial Aerodynamics*, 69, 1997, pp.819-827.
24. Bruno, L., Mancini, G., "Importance of deck details in bridge aerodynamics". *Structural Engineering International*, 12(4), 2002, pp.289-294.
25. Xu, F. Y., Li, B. B., Cai, C. S., Asce, F., Zhang, Z., "Experimental investigations on aerostatic characteristics of bridge decks under various conditions". *Journal Of Bridge Engineering*, 19(7), 2014, pp.27-35.
26. Zhou, G. D., Yi, T. H., Chen, B., Zhang, H., "A generalized pareto distribution-based extreme value model of thermal gradients in a long-span bridge combining parameter updating". *Advances in Structural Engineering*, 20(2), 2017, pp.202-213.
27. Nieto, F., Owen, J. S., Hargreaves, D. M., Hernández, S., "Bridge deck flutter derivatives: Efficient numerical evaluation exploiting their interdependence". *Journal of Wind Engineering and Industrial Aerodynamics*, 136, 2015, pp.138-150.
28. Durrani, F., Cook, M. J., McGuirk, J. J., "Evaluation of les and rans CFD modelling of multiple steady states in natural ventilation". *Building and Environment*, 92, 2015, pp.167-181.